

Article

Open Access



Impact of intergranular phase variations on the anomalous Nernst effect in Nd-Fe-B permanent magnets

Zulfa Hilmi Kautsar^{1,2}, Babu Madavali², Takamasa Hirai², Ken-ichi Uchida^{1,2,3}, Hossein Sepehri-Amin^{1,2,*}

¹Graduate School of Science and Technology, University of Tsukuba, Tsukuba 305-8577, Japan.

²National Institute for Materials Science (NIMS), Tsukuba 305-0047, Japan.

³Department of Advanced Materials Science, Graduate School of Frontier Sciences, The University of Tokyo, Kashiwa 277-8561, Japan.

*Correspondence to: Prof. Hossein Sepehri-Amin, Research Center for Magnetic and Spintronic Materials, National Institute for Materials Science (NIMS), Sengen 1-2-1, Tsukuba 305-0047, Japan. E-mail: h.sepehriamin@nims.go.jp

How to cite this article: Kautsar, Z. H.; Madavali, B.; Hirai, T.; Uchida, K.; Sepehri-Amin, H. Impact of intergranular phase variations on the anomalous Nernst effect in Nd-Fe-B permanent magnets. *Energy Mater.* **2025**, *5*, 500129. <https://dx.doi.org/10.20517/energymater.2025.26>

Received: 29 Jan 2025 **First Decision:** 18 Mar 2025 **Revised:** 18 Apr 2025 **Accepted:** 30 Apr 2025 **Published:** 26 Jun 2025

Academic Editor: Sining Yun **Copy Editor:** Ping Zhang **Production Editor:** Ping Zhang

Abstract

Improving the anomalous Nernst coefficient (S_{ANE}) in permanent magnets is essential for increasing the power density in transverse thermoelectric generators, which use permanent magnets to operate the anomalous Nernst effect without relying on an external magnetic field. While recent studies indicate that microstructural engineering can affect S_{ANE} , the specific relationship between microstructure and S_{ANE} in permanent magnets remains underexplored. This study investigates S_{ANE} of hot-pressed, hot-deformed, and RE-Cu (RE = Dy-Nd, Nd, and Pr) grain boundary diffusion-processed Nd-Fe-B magnets. The results show that S_{ANE} increases by 68%, from $-2.6 \times 10^{-7} \text{ VK}^{-1}$ in the hot-pressed state to $-4.4 \times 10^{-7} \text{ VK}^{-1}$ after hot-deformation in which grain growth and crystallographic texture are realized without changing the composition of the magnets. S_{ANE} further increases to $-5.0 \times 10^{-7} \text{ VK}^{-1}$ after grain boundary structure and composition change from thin amorphous phase to thick crystalline phase by grain boundary diffusion of Dy-Nd-Cu alloy. The increase in S_{ANE} is found to be primarily due to the reduction of the opposing transverse electric field caused by the Seebeck-effect-induced carrier flow bent by the anomalous Hall effect. Owing to the crystallographic texture formation after hot-deformation, almost the same transverse thermopower as S_{ANE} is obtained in the hot-deformed and RE-Cu grain boundary diffusion-processed Nd-Fe-B magnets at a remanence state, i.e., under zero magnetic field. These findings demonstrate that microstructural optimization can effectively enhance the S_{ANE} in ultra-fine grained Nd-Fe-B magnets, providing a promising avenue for advancing materials in applications of transverse thermoelectrics.

Keywords: Anomalous Nernst effect, hot-deformed magnets, microstructural engineering, Nd-Fe-B, permanent magnets



© The Author(s) 2025. **Open Access** This article is licensed under a Creative Commons Attribution 4.0 International License (<https://creativecommons.org/licenses/by/4.0/>), which permits unrestricted use, sharing, adaptation, distribution and reproduction in any medium or format, for any purpose, even commercially, as long as you give appropriate credit to the original author(s) and the source, provide a link to the Creative Commons license, and indicate if changes were made.



INTRODUCTION

Thermoelectric technology enables the conversion of heat into electricity, and vice versa, offering a promising alternative to meet the growing demand for sustainable energy. Conventional thermoelectric generators (TEGs) operate based on the Seebeck effect, a longitudinal thermoelectric phenomenon where the induced electric field aligns parallel to the temperature gradient. As a result, optimizing thermoelectric output in Seebeck-based TEGs necessitates multiple legs of *p*- and *n*-type semiconductors connected in series, typically arranged in a Π -shaped configuration^[1,2]. However, constructing this Π -shaped configuration involves numerous electrode junctions, leading to potential drawbacks such as a low fill factor^[3,4], high power loss^[5], and reduced device durability^[6].

An alternative approach is to develop TEGs based on the transverse thermoelectric effect, where the induced electric field is perpendicular to the temperature gradient. This reduces the number of required junctions, simplifying the TEG design and addressing the limitations of conventional longitudinal TEGs. An important transverse thermoelectric effect for power generation is the Nernst effect. The Nernst effect generates a charge current perpendicular to both the temperature gradient and either an applied magnetic field (*H*) or the material's magnetization (*M*), referring to as the ordinary Nernst effect (ONE) when driven by *H*, or as the anomalous Nernst effect (ANE) when driven by the *M* of the material. A major limitation of both ONE and ANE in many materials is the need to apply a continuous H ^[7-21], which complicates their application in TEGs. To achieve zero-field operation in transverse Nernst-based TEGs, it is essential to achieve high thermoelectric conversion performance of ANE in magnetic materials with high coercivity (H_c) and remanent magnetization (M_r), such as permanent magnets, and integrate them into TEG devices. Another viable approach is to utilize ONE and ANE with other transverse thermoelectric effects, such as the off-diagonal Seebeck/Peltier effect^[22,23].

Among the currently available permanent magnets, Nd-Fe-B and Sm-Co-based magnets exhibit high H_c and M_r at room temperature^[24-26]. Miura *et al.*^[27] observed a significant positive anomalous Nernst coefficient (S_{ANE}) in the SmCo₅-based sintered magnets ($+3.5 \times 10^{-6} \text{ VK}^{-1}$) and negative S_{ANE} ($-8.7 \times 10^{-7} \text{ VK}^{-1}$) in the Nd₂Fe₁₄B-based sintered magnets. By combining these two permanent magnets, Ando *et al.*^[1] developed a transverse TEG device with a high fill factor that achieved an ANE-driven power generation (power density) of 177 μW ($65 \mu\text{Wcm}^{-2}$) at a temperature difference of 75 K, using a 273 K heat sink, the record-high value among transverse TEGs utilizing ANE. However, this value is still a few orders of magnitude lower than that of conventional Seebeck-based TEGs. Therefore, enhancing the S_{ANE} value of the permanent magnets is crucial and requires fundamental research that focuses not only on exploring new materials but also on advancing our understanding of microstructural factors.

Many efforts to enhance S_{ANE} in magnetic materials are aimed at optimizing the Berry curvature contribution in electronic band structures^[20,28,29]. In contrast, recently, Gautam *et al.*^[30] demonstrated a new direction for improving S_{ANE} from the viewpoint of microstructure engineering. The formation of nonmagnetic copper nanoclusters in an amorphous ferromagnetic Fe-based matrix was shown to enhance both electrical conductivity (σ_{xx}) and thermal conductivity (κ) of the alloys, with an optimal nanocluster size increasing the S_{ANE} value by 70%. This raises the question of how microstructure engineering, traditionally employed to optimize coercivity and remanence in the permanent magnets^[31-35], influences their σ_{xx} , κ , and S_{ANE} .

This study aims to investigate how variations in grain size and intergranular phase (IGP) influence σ_{xx} , κ , and S_{ANE} in the Nd-Fe-B permanent magnets. These magnets were fabricated from rapidly solidified Nd-Fe-B ribbon powders with an initial nano-sized grain structure^[36,37]. During the different processing stages of hot-pressing, hot-deformation, and grain boundary diffusion process (GBDP), significant microstructural changes occur^[38-41], which will be systematically analyzed. The findings are expected to shed light on the relationship between microstructural evolution and transport properties in the Nd-Fe-B magnets, contributing to the design and optimization of permanent magnet materials for transverse thermoelectric applications.

EXPERIMENTAL

Nd-Fe-B magnets preparation

The starting material used in this study was a commercial Nd-Fe-B crushed melt-spun ribbon powder, MQU-F, with the composition of Nd_{13.6}Fe_{73.6}Co_{6.6}Ga_{0.6}B_{5.6} (at%), supplied by Magnequench Co. Ltd. The MQU-F powder was first hot-pressed at 650 °C under 300 MPa to produce a hot-pressed (HP) compact. This HP compact was then hot-deformed at 750 °C with a 75% height reduction, resulting in an anisotropic hot-deformed (HD) magnet. To produce GBDP magnets, alloy ribbon flakes of Dy₂₀Nd₆₀Cu₂₀ (at%), Nd₈₀Cu₂₀ (at%), and Pr₈₀Cu₂₀ (at%) were prepared using a single-roll melt-spinning machine, followed by mechanical crushing. These diffusion sources were chosen based on prior reports demonstrating their effectiveness in achieving high coercivity in the ultra-fine grained Nd-Fe-B magnets^[39-41]. Due to the limited studies on the impact of GBDP on ANE performance, this factor was not considered in the selection process. The *c*-plane surfaces of the HD magnet (2 mm thick) were coated by diffusion sources in the form of ribbon flakes (~20 wt%) using a polymer adhesive. The magnets were then heat-treated at 650-750 °C for 3 h under vacuum, followed by furnace cooling to ambient temperature, resulting in RE-Cu (RE = Dy-Nd, Nd, Pr) GBDP HD magnets.

Characterization and measurements

Microstructural analysis was conducted using Scanning Electron Microscopy (SEM, Carl ZEISS CrossBeam 1540EsB) and Transmission Electron Microscopy (TEM, FEI Titan G2 80-200). Sample preparation for these analyses was carried out using a focused ion beam (FIB)-SEM device (FEI Helios G4). The magnets were sectioned into specific sample dimensions to suit each type of measurement, with the *c*-axis indicating the easy magnetization direction of the magnet (if applicable): 1.5 mm (*c*-axis) × 1.0 mm × 1.0 mm for magnetic property measurements, 2 mm (*c*-axis) × 2 mm × 15 mm for σ_{xx} and thermoelectric measurements, 1.5 mm (*c*-axis) × 10 mm × 10 mm for thermal diffusivity (D_t) measurements, and 0.5 mm (*c*-axis) × 1 mm × 5 mm for Hall measurements. Magnetic properties were evaluated by measuring the magnetization curves of the samples using a 7 T superconducting quantum interference device vibrating sample magnetometer (SQUID-VSM, Quantum Design MPMS3). A demagnetization correction factor for a prism-shaped magnet, as described in ref.^[42], was applied to the measured hysteresis loop to account for the open-loop measurement. This resulted in a correction factor of 0.25 for the sample used in magnetic property measurements and 0.47 for the samples used in lock-in thermography (LIT) measurements. Grain alignment was assessed using X-ray diffraction (XRD, Rigaku MiniFlex600, Cr K α source) by analyzing the surface normal to the pressing direction for all bulk samples. The values of σ_{xx} and the Seebeck coefficient (S_{xx}) were simultaneously determined using Seebeck Coefficient/Electric Resistance Measurement System (ZEM-3, ADVANCE RIKO, Inc.). To quantify S_{ANE} , we measured the anomalous Ettingshausen effect (AEE), Onsager reciprocal of ANE, using the LIT method^[27,43-48]. The LIT technique, based on infrared thermometry, enables high-resolution observation of temporal response and spatial distribution induced by an external periodic input, with exceptional sensitivity (< 0.1 mK) and spatial resolution (~20 μ m)^[23]. In the LIT measurements, the thermal images were captured using an infrared camera while applying a square-wave modulated AC charge current with amplitude $J_c = 1.0$ A, frequency $f = 1.0$ -10.0 Hz, and zero

offset to the slabs along the longitudinal direction of the sample's long side, perpendicular to the magnet's c -axis. The first harmonic of the detected thermal images was extracted and subjected to Fourier analysis to determine the lock-in amplitude (A) and phase (ϕ). Using this process, the pure contribution of thermoelectric response, i.e., AEE and the Peltier effect, can be detected free from Joule heating. The A image represents the magnitude of current-induced temperature modulation, while the ϕ image indicates the sign of the temperature modulation and the time delay caused by thermal diffusion. To enhance the infrared emissivity, the top surface of the samples was coated with insulating black ink of which the infrared emissivity is > 0.94 . The LIT measurements were conducted in the M_r state without applying H , where the magnets were magnetized along the c -axis. The detected infrared radiation intensity is converted to temperature values through the calibration process described in ref.^[44]. Since the AEE-induced temperature modulation exhibits the H -odd dependence, the H -odd-dependent component of the lock-in amplitude A_{odd} and the phase ϕ_{odd} were evaluated using $A_{\text{odd}} = |A(+M_r)e^{-i\phi(+M_r)} - A(-M_r)e^{-i\phi(-M_r)}|/2$ and $\phi_{\text{odd}} = -\arg[A(+M_r)e^{-i\phi(+M_r)} - A(-M_r)e^{-i\phi(-M_r)}]$, where $A(+M_r)$ [$\phi(+M_r)$] and $A(-M_r)$ [$\phi(-M_r)$] show the A (ϕ) value measured at the sample M of $+M_r$ and $-M_r$, respectively. The M reversal process was performed by applying a 3T H in the opposing direction to the sample slabs. D_i was measured using the laser flash method. κ was then estimated by multiplying the D_i value with the specific heat capacity (c_p) obtained from differential scanning calorimetry (DSC, Rigaku Thermo Plus EV02) and the density determined using the Archimedes method. The Hall measurement was performed to estimate the transverse electrical resistivity (ρ_{yx}) using a physical property measurement system (PPMS, Quantum Design, Inc.).

RESULTS AND DISCUSSION

Figure 1A presents the magnetization curves of the HP and HD samples, with the y -axis representing M and the x -axis corresponding to H . The y -intercept of the graph corresponds to M_r , which represents the sample M at zero H . The saturation magnetization (M_s) of the samples was measured under the maximum H . The HP sample displays a low remanence to saturation magnetization ratio (M_r/M_s) of 0.63 and a slightly rounded demagnetization curve in the second quadrant which is a typical feature for the isotropic permanent magnets. In contrast, the HD sample shows an increase in the M_r/M_s ratio to 0.94, indicating a large degree of texture in the studied magnet^[49]. Furthermore, the demagnetization curves become more square-shaped, reflecting a substantial enhancement in the crystallographic texture of the $\text{Nd}_2\text{Fe}_{14}\text{B}$ grains after hot-deformation. Consequently, the $\mu_0 M_r$ of the magnet improves significantly, increasing from 0.72 T in the HP state to 1.30 T in the HD state.

Figure 1B presents the magnetization curves for the Dy-Nd-Cu, Nd-Cu, and Pr-Cu GBDP magnets, with the HD magnet included for comparison. These magnets retain the anisotropic loop shape, though their M is reduced due to the dilution of $\text{Nd}_2\text{Fe}_{14}\text{B}$ phase after the diffusion process. $\mu_0 M_r$ values for the Dy-Nd-Cu, Nd-Cu, and Pr-Cu GBDP magnets are 1.01, 0.99, and 1.06 T, respectively. In contrast, their $\mu_0 H_c$ increases significantly, rising from 1.00 T in the initial HD magnet to 2.28 T, 1.62 T, and 1.85 T after the Dy-Nd-Cu, Nd-Cu, and Pr-Cu diffusion process, respectively. The corresponding values of $\mu_0 M_r$, $\mu_0 M_s$, M_r/M_s , $\mu_0 H_c$, and maximum energy product $(BH)_{\text{max}}$ for each magnet are given in Supplementary Table 1 of the supplementary information.

Supplementary Figure 1 presents the XRD patterns of the studied magnets. In the HP magnets, the (410), (214), and (330) reflections dominate, indicating a random grain orientation. After HD, however, the (006), (105), and (004) reflections become prominent, signifying strong c -axis crystallographic alignment^[50,51]. This high degree of alignment is preserved after GBDP, as evident in the XRD of Dy-Nd-Cu, Nd-Cu, and Pr-Cu magnets and in agreement with M_r/M_s ratio data [Supplementary Table 1].

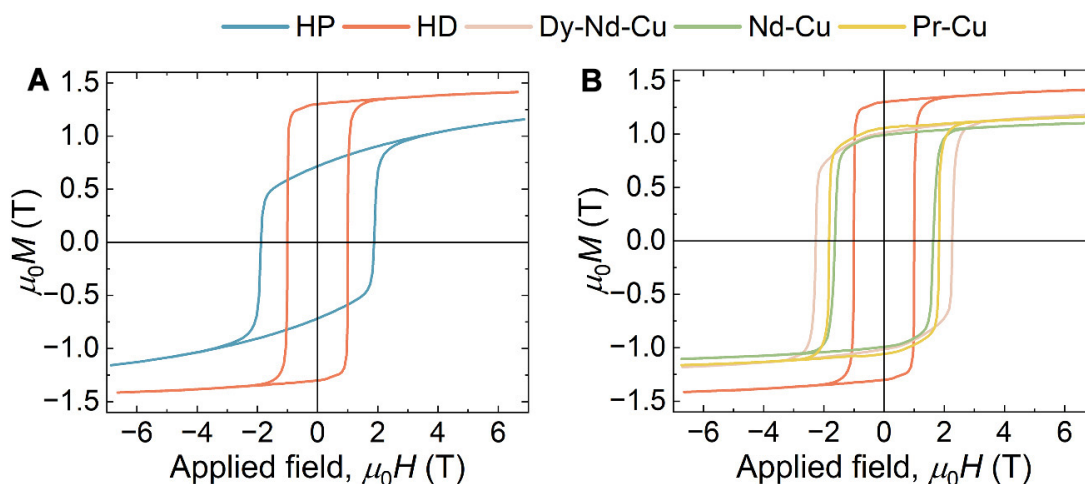


Figure 1. (A) Magnetization curves of HP and HD magnets, showing the transition from isotropic to anisotropic magnetic properties; (B) Magnetization curves of HD magnets after Dy-Nd-Cu, Nd-Cu, and Pr-Cu GBDP, illustrating retained anisotropy with varying coercivity enhancements. HP: Hot-pressed; HD: hot-deformed; GBDP: grain boundary diffusion process.

To investigate the microstructural changes following processing, microstructural analyses were conducted on the studied magnets. Due to differences in grain size, the HP magnet was examined using TEM [Figure 2A], while the HD and GBDP HD magnets were observed using SEM [Figure 2B-E]. A backscattered electron scanning electron microscopy (BSE-SEM) image of the HP magnet is provided in Supplementary Figure 2 to illustrate the difficulty of observing its fine-grained structure using SEM. The HP magnet [Figure 2A] exhibits fine, equiaxed grains with sizes less than 100 nm. These isotropic grains contribute to the low M_r/M_s ratio observed in Figure 1A. After HD [Figure 2B], the $\text{Nd}_2\text{Fe}_{14}\text{B}$ grains evolve into well-aligned, platelet-like grains with sizes exceeding 200 nm in lateral direction. Note that the brightly imaged regions in BSE-SEM images indicate the presence of a Nd-rich phase existing in the grain boundary region of the HD sample. This microstructural transformation explains the increase in the M_r/M_s ratio after HD [Figure 1A], which shifts the magnet's characteristics from isotropic to anisotropic. The observed anisotropic grains after HD is consistent with the previous reports^[38]. However, unlike in^[38], platelet-shaped grains were not observed in the HP magnet in this study, likely due to the short duration (less than five minutes) of the hot pressing process.

Figure 2C-E illustrates the microstructures of the RE-Cu (RE = Dy-Nd, Nd, Pr) GBDP magnets. These images reveal a significant change in the thickness of RE-rich IGP following RE-Cu GBDP, evident from the increased areal fraction of the bright phase in BSE-SEM images, from 6% in the HD magnet [Figure 2B] to 20%, 19%, and 28% after Dy-Nd-Cu, Nd-Cu, and Pr-Cu GBDP, respectively [Figure 2C-E]. The formation of a thick RE-rich IGP, which magnetically isolates $\text{Nd}_2\text{Fe}_{14}\text{B}$ grains, is known to enhance coercivity in the GBDP magnets^[39-41]. In addition, grain misorientations and the increased volume fraction of the IGP observed in the RE-Cu GBDP magnets likely account for the reduced M_r in these magnets, as presented in Figure 1B.

We investigated the microstructure and the distribution of constituent and diffused elements in HD and RE-Cu (RE = Dy-Nd, Nd, Pr) GBDP magnets using high-angle annular dark field (HAADF)-scanning transmission electron microscopy (STEM) and STEM-energy dispersive X-ray spectroscopy (EDS) techniques [Figure 3A-D]. Our observations revealed an increase in thickness and segregation of RE-Cu elements within the IGP of the GBDP magnets. Additionally, we identified the formation of $(\text{Nd,Dy})_2\text{Fe}_{14}\text{B}$

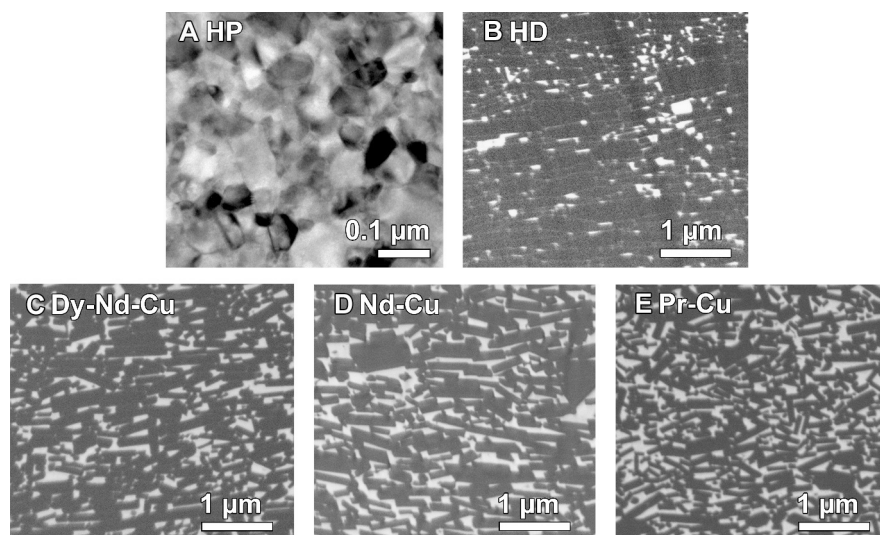


Figure 2. (A) BF-TEM image of the hot-pressed (HP) magnet; along with BSE-SEM images of (B) the hot-deformed (HD) magnet; (C) Dy-Nd-Cu grain boundary diffusion processed (GBDP); (D) Nd-Cu GBDP; and (E) Pr-Cu GBDP HD magnets. BSE-SEM: Backscattered electron scanning electron microscopy; BF-TEM: bright-field transmission electron microscopy.

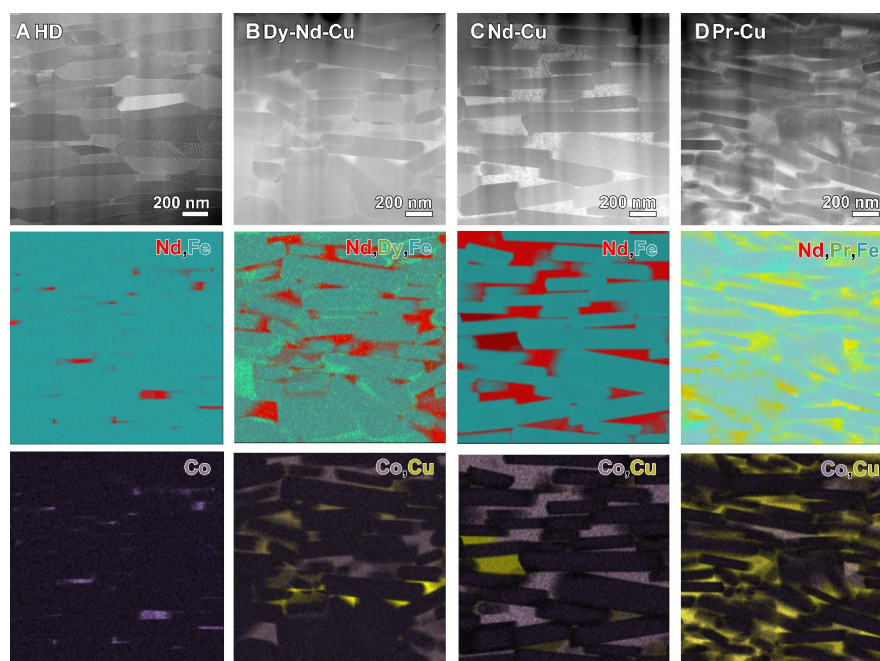


Figure 3. STEM-HAADF images and STEM-EDS elemental maps showing the distribution of constituent and diffused elements for (A) the HD magnet; (B) the Dy-Nd-Cu GBDP HD magnet; (C) the Nd-Cu GBDP HD magnet; and (D) the Pr-Cu GBDP HD magnet. HD: Hot-deformed; GBDP: grain boundary diffusion process; STEM-HAADF: high-angle annular dark field scanning transmission electron microscopy; STEM-EDS: STEM-energy dispersive X-ray spectroscopy.

and $(\text{Nd,Pr})_2\text{Fe}_{14}\text{B}$ phase on the outer surfaces of $\text{Nd}_2\text{Fe}_{14}\text{B}$ grains in the Dy-Nd-Cu and Pr-Cu GBDP magnets, respectively [Figure 3B and D]. Since $\text{Dy}_2\text{Fe}_{14}\text{B}$ and $\text{Pr}_2\text{Fe}_{14}\text{B}$ exhibit larger magnetic anisotropy fields than $\text{Nd}_2\text{Fe}_{14}\text{B}$ at room temperature^[52], the formation of Dy-rich and Pr-rich shell regions in the Dy-Nd-Cu and Pr-Cu GBDP magnets contributes to a higher coercivity compared to the Nd-Cu GBDP magnet.

Figure 4A summarizes the σ_{xx} of the studied magnets, showing a slight increase after HD and subsequent GBDP. No notable differences in σ_{xx} were observed among the RE-Cu (RE = Dy-Nd, Nd, Pr) GBDP magnets. Figure 4B presents the κ and the lattice contribution to thermal conductivity (κ_{lat}) of the studied magnets. The κ_{lat} is extracted by subtracting the electronic contribution (κ_e) from the total κ_{lat} : $\kappa_{lat} = \kappa - \kappa_e$. The κ_e is estimated using the Wiedemann-Franz Law $\kappa_e = L\sigma_{xx}T$, where L represents the Lorenz number ($2.44 \times 10^{-8} \text{ W}\Omega\text{K}^{-2}$) and T is the absolute temperature^[30]. Figure 4B shows that the κ_{lat} exhibits a slight increase after HD but rises significantly following GBDP. This contributes to the increase in κ in the HD and GBDP magnets compared to the HP magnet. The κ_e values of the studied magnets are presented in Supplementary Figure 3; κ_e shows only a slight increase after HD and GBDP.

The observed increase in σ_{xx} and κ following HD and GBDP can be attributed to the grain growth^[53,54]. However, the substantial rise in κ_{lat} after GBDP suggests the involvement of an additional mechanism. To investigate this, microstructural analyses comparing the IGP of HP, HD and GBDP magnets-represented by the Dy-Nd-Cu GBDP magnet-were conducted, as illustrated in Figure 5A-C. The HP magnet exhibits a thin amorphous IGP [Figure 5A], which is retained in the HD magnet [Figure 5B]. However, this phase transforms into a thick crystalline IGP after GBDP [Figure 5C and D]. This crystallization of the IGP after GBDP is likely a key factor driving the pronounced increase in κ_{lat} , as crystalline IGPs typically exhibit higher phonon mean free paths and reduced phonon scattering compared to their amorphous counterparts, thereby improving κ ^[30,55,56]. Additionally, the prolonged heat treatment during GBDP may also contribute to the increase in κ_{lat} by reducing point defect scattering. The reduced content of ferromagnetic elements (Fe + Co) in the IGP after GBDP contributes to the enhanced coercivity [Figure 1B] by reducing the M of the IGP^[39-41,57]. However, the impact of this compositional change on σ_{xx} and κ still requires further investigation. The mechanism of IGP thickening and crystallization can be described as follows. During GBDP, the diffusion source, consisting of eutectic alloys, melts and infiltrates the magnet through the grain boundaries. This process increases the thickness and volume fraction of the RE-rich phase in the IGP and modifies its composition. The thickening of the IGP during GBDP, combined with prolonged annealing, likely explains the observed crystallization.

Here we show the transverse thermoelectric conversion properties of the studied magnets. Figure 6A presents the A_{odd} and ϕ_{odd} images of the studied magnets at $f = 1.0 \text{ Hz}$ and $J_c = 1.0 \text{ A}$, measured in the M_r state under zero H . Uniform current-induced temperature modulation is clearly observed across the entire surface of the magnet slabs. To quantitatively estimate the anomalous Ettingshausen coefficient Π_{AEE} ($=S_{ANE}T$), the A_{odd} per unit charge current density j_c , i.e., A_{odd}/j_c , was measured at different f ranging from 1.0 Hz to 10.0 Hz , as shown in Figure 6B. The A_{odd} values at each f were obtained by averaging the A_{odd} values over the marked rectangular area ($1.2 \times 4.5 \text{ mm}^2$) in Figure 6A. A clear decrease in A_{odd}/j_c with increasing f was observed, which is well replicated by considering thermal diffusion in the sample using the one-dimensional heat diffusion equation in the frequency domain (solid lines in Figure 6B)^[27]. Finally, the steady-state value of A_{odd}/j_c corresponding to $f \rightarrow 0 \text{ Hz}$ ($A_{odd,0\text{Hz}}/j_c$), was calculated from fitting the curve in Figure 6B. The signal with ϕ_{odd} approximately 180° indicates that the bottom surface of the sample ($-y$ direction) is being heated, as illustrated in Figure 6C.

The Π_{AEE} and S_{ANE} values were calculated using $\Pi_{AEE} = S_{ANE}T = \frac{\kappa|\Delta T_{AEE}|}{J_c L}$, where L is the sample thickness and ΔT_{AEE} represents the temperature difference between the top and bottom surfaces of the sample induced by AEE. This temperature difference is determined as $\Delta T_{AEE} = 2A_{odd,0\text{Hz}}(M_s/M_r)^{[45]}$. An M_s/M_r correction is applied to address the incomplete saturation of the studied magnets' M during the AEE measurements. To ensure accurate determination of the M_s/M_r values for the LIT sample slabs, their magnetic hysteresis loops were measured using a pulse B - H tracer [Supplementary Figure 4], and the results are summarized in

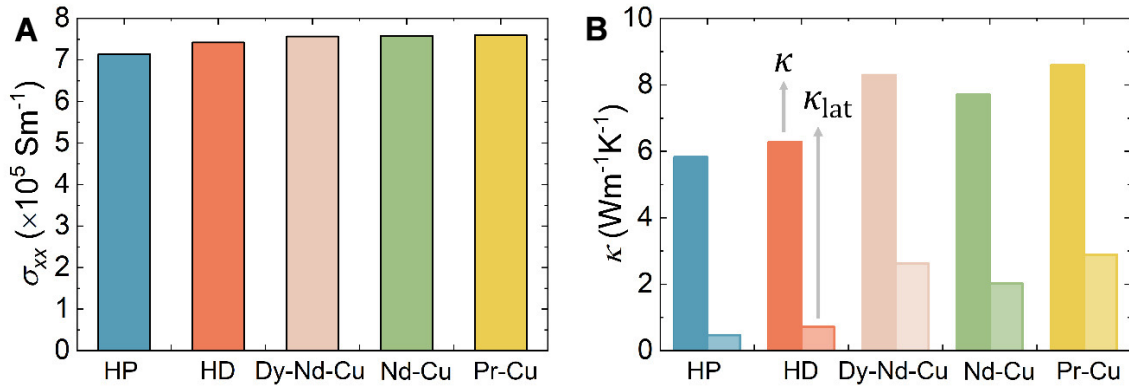


Figure 4. (A) Electrical conductivity (σ_{xx}) and (B) total thermal conductivity (κ) and lattice thermal conductivity (κ_{lat}) of the HP, HD, and RE-Cu (RE = Dy-Nd, Nd, Pr) GBDP HD magnets. HP: Hot-pressed; HD: hot-deformed; GBDP: grain boundary diffusion process.

Supplementary Table 2. The estimated values of Π_{AEE} and S_{ANE} are summarized in **Figure 6D**. The Π_{AEE} (S_{ANE}) increases from $-7.9 \times 10^{-5} \text{ V}$ ($-2.6 \times 10^{-7} \text{ VK}^{-1}$) in the HP state to $-1.3 \times 10^{-4} \text{ V}$ ($-4.4 \times 10^{-7} \text{ VK}^{-1}$) after HD. Further GBDP using Dy-Nd-Cu results in additional increments, reaching to $-1.5 \times 10^{-4} \text{ V}$ ($-5.0 \times 10^{-7} \text{ VK}^{-1}$). It is worth noting that, due to the crystallographic texture formed during hot-deformation, the transverse thermopower at the M_r state (zero H) in HD and RE-Cu (RE = Dy-Nd, Nd, and Pr) GBDP Nd-Fe-B magnets is nearly identical (85%-86%) to that of S_{ANE} .

The transverse thermoelectric conversion performance of ANE was evaluated using the dimensionless figure of merit, $z_{\text{ANE}}T$, expressed as $\frac{S_{\text{ANE}}^2 \sigma_{xx} T}{\kappa}$ [45]. As shown in **Figure 6E**, $z_{\text{ANE}}T$ increases significantly after HD, primarily due to the substantial rise in S_{ANE} . However, while GBDP further enhances S_{ANE} , the concurrent increase in κ partially counterbalanced this improvement, resulting in slight increment in $z_{\text{ANE}}T$ for the Dy-Nd-Cu and Pr-Cu GBDP magnets. The highest $z_{\text{ANE}}T$ value achieved in this study is 8.1×10^{-6} , observed in the Nd-Cu GBDP magnet.

S_{ANE} can be decomposed into two components: $S_{\text{ANE}} = \rho_{xx} \alpha_{xy} - \rho_{\text{AHE}} \alpha_{xx} \equiv S_{\text{I}} + S_{\text{II}}$ [6,28]. Here, ρ_{xx} ($= 1/\sigma_{xx}$) is the longitudinal electrical resistivity, α_{xy} is the transverse thermoelectric conductivity, ρ_{AHE} is the anomalous Hall resistivity, and α_{xx} is the longitudinal thermoelectric conductivity. The S_{I} component reflects the direct conversion of a temperature gradient into a transverse electric field through α_{xy} . In contrast, the S_{II} component represents the transverse electric field due to the Seebeck-effect-induced carrier flow bent by anomalous Hall effect (AHE). S_{II} can be rewritten as $S_{\text{II}} = -\frac{\rho_{\text{AHE}}}{\rho_{xx}} \alpha_{xx} \rho_{xx} = -\tan \theta_{\text{AHE}} S_{xx}$, where θ_{AHE} is the anomalous Hall angle.

The S_{xx} values of the studied magnets are shown in **Figure 7A**. All the magnets exhibit negative S_{xx} values, with the absolute values decreasing after HD and subsequent GBDP. **Figure 7B** shows the ρ_{yx} as a function of the H for the studied magnets. It is worth mentioning that the ρ_{yx} curve follows the magnetization curves of the magnets and the slope of ρ_{yx} as a function of external magnetic field becomes negligible after saturation of magnetization [Figure 7B]. This suggests that the ordinary Hall contribution to the ρ_{yx} is negligible compared to anomalous Hall contribution in the present study [58]. Additionally, the graph exhibits H -odd symmetry characteristic, as it is symmetric with respect to the origin. This indicates that the magneto-Seebeck effect also contributes negligibly. The ρ_{AHE} is determined by extrapolating ρ_{yx} at $\mu_0 H = 14 \text{ T}$ to the zero field. **Supplementary Figure 5** presents the ρ_{AHE} values and the anomalous Hall angle ($\tan \theta_{\text{AHE}}$) of the studied magnets. The absolute values of ρ_{AHE} and $\tan \theta_{\text{AHE}}$ are gradually decreased after GBDP. Notably, although ρ_{AHE} slightly decreases after HD, $\tan \theta_{\text{AHE}}$ increases. Further studies are required to clarify the

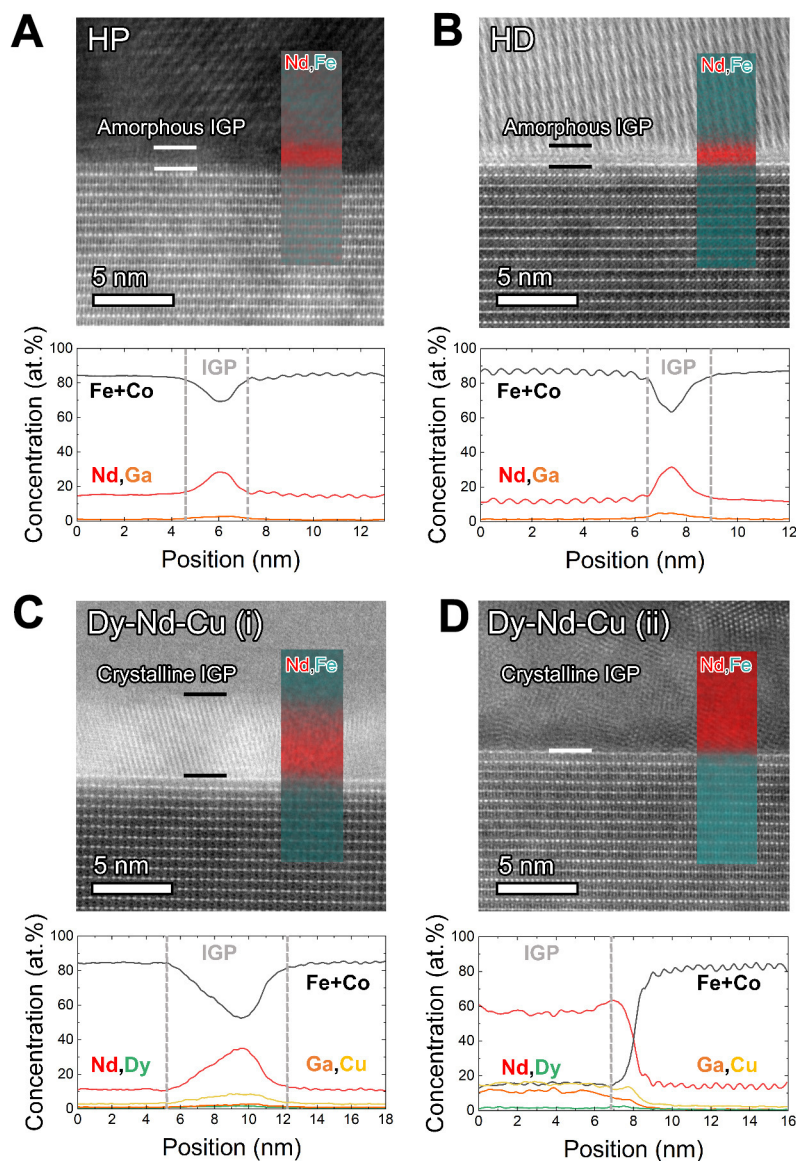


Figure 5. High resolution HAADF-STEM images and superimposed STEM-EDS maps of Nd and Fe obtained across the intergranular phase (IGP) region in (A) HP, (B) HD, and (C and D) Dy-Nd-Cu GBDP HD magnets, along with the corresponding concentration depth profiles of Nd, Fe, Co, Dy, and Cu. HP: Hot-pressed; HD: hot-deformed; GBDP: grain boundary diffusion process; STEM-HAADF: high-angle annular dark field scanning transmission electron microscopy; STEM-EDS: scanning transmission electron microscopy - energy dispersive X-ray spectroscopy.

underlying mechanism of these changes. Figure 7C presents the contributions of S_I and S_{II} to the total S_{ANE} of the studied magnets. All the Nd-Fe-B magnets show comparable magnitudes for S_I and S_{II} , but with opposite signs. The S_I values for the studied magnets remain relatively constant after HD and GBDP, with slight reductions observed in the Nd-Cu and Pr-Cu GBDP magnets. In contrast, the S_{II} values exhibit a clear and significant decrease as the magnets undergo HD and GBDP, which correlates with the substantial changes in S_{xx} and ρ_{yx} [Figure 7A and B] observed following these treatments. This result suggests that microstructural changes following HD and GBDP of rapidly solidified Nd-Fe-B magnets have a more pronounced effect on S_{II} than on S_I . The reduction of the opposing S_{II} was observed alongside grain growth and crystallographic texture formation resulting from HD, as well as the transformation of the amorphous

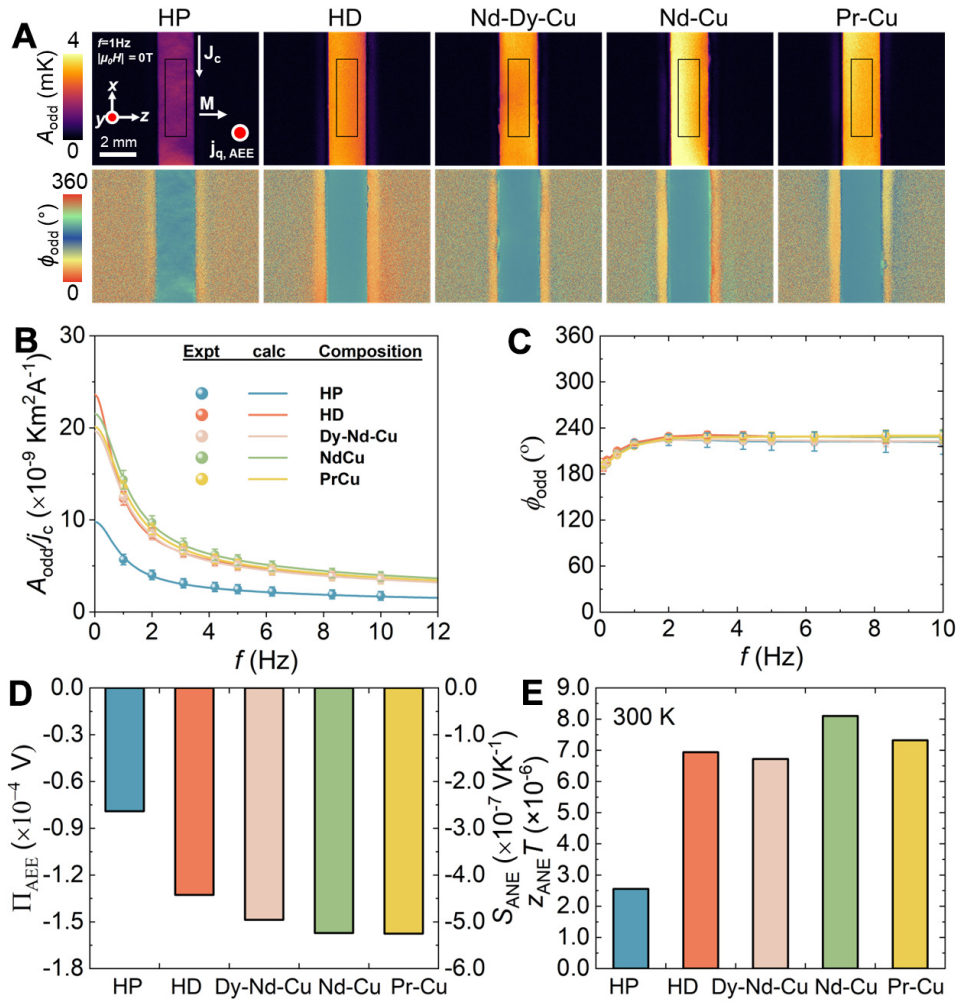


Figure 6. (A) A_{odd} and ϕ_{odd} images at $J_c = 1.0 \text{ A}$, and $f = 1 \text{ Hz}$ for HP, HD, and RE-Cu (RE = Dy-Nd, Nd, Pr) GBDP HD magnets; (B) Frequency dependence of the A_{odd}/I_c (C) ϕ_{odd} (D) Π_{AEE} and S_{ANE} , (E) $z_{\text{ANE}} T$ for same studied magnets. HP: Hot-pressed; HD: hot-deformed; GBDP: grain boundary diffusion process; S_{ANE} : anomalous nernst coefficient; AEE: anomalous Ettingshausen effect.

IGP into a crystalline phase after GBDP. This reduction leads to an increase in the total S_{ANE} . The α_{xy} , which is often used to evaluate the thermoelectric performance of ANE, is shown in Figure 7D. It can be seen that the absolute value of α_{xy} only experiences a slight increase after HD and a slight decrease after GBDP, indicating that it remains relatively unchanged throughout these processes.

Finally, we discuss potential strategies to further enhance the S_{ANE} and $z_{\text{ANE}} T$ of Nd-Fe-B permanent magnets. Based on this study and previous work on commercial sintered magnets^[27], we observe that the contributions from S_{I} and S_{II} in Nd-Fe-B magnets tend to have opposite signs, leading to a small S_{ANE} due to the destructive summation of the two components. The formation of crystalline IGP in Nd-Fe-B magnets could potentially increase S_{ANE} by reducing the S_{II} magnitude or changing its sign. However, this increase in S_{ANE} is somewhat offset by the rise in κ resulting in a smaller enhancement of $z_{\text{ANE}} T$. To further enhance both S_{ANE} and $z_{\text{ANE}} T$ in Nd-Fe-B magnets, it is also necessary to increase the S_{I} component, without significantly increasing κ . This can be achieved by enhancing α_{xy} , which is fundamentally tied to the Berry curvature at the Fermi level^[59,60]. Tuning the Berry curvature near the Fermi level or equivalently, tuning the Fermi level position, has been shown to effectively enhance the transverse thermoelectric coefficient α_{xy} , as

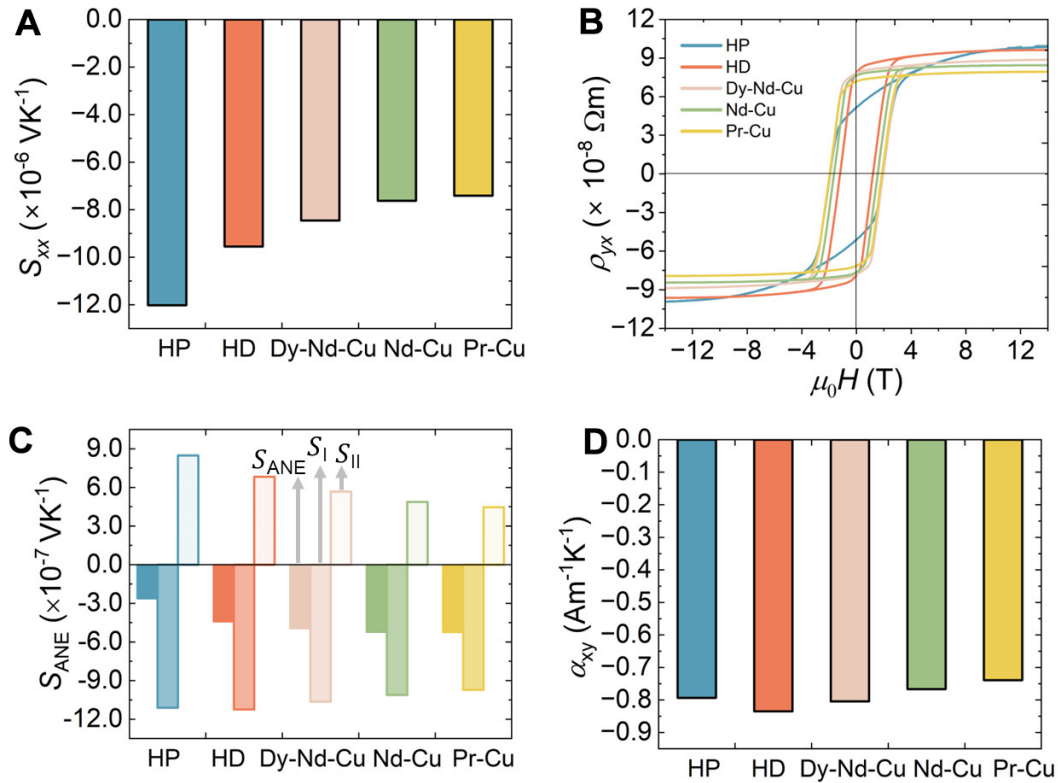


Figure 7. (A) Seebeck coefficient (S_{xx}); (B) $\mu_0 H$ dependence of Hall resistivity (ρ_{yx}); (C) contributions of S_I and S_{II} to the S_{ANE} ; and (D) transverse thermoelectric conductivity (α_{xy}) for the studied magnets. S_{ANE} : Anomalous nernst coefficient.

demonstrated in ref.^[28,61]. On the other hand, a systematic investigation of microstructural features beyond the crystallinity of the IGP, including grain size, shape, IGP thickness, and IGP continuity is still needed to understand how they impact the S_I and S_{II} components. Although the S_{ANE} of the magnets studied in this research is still lower than that of commercial sintered magnets reported in previous work^[27], as shown in [Supplementary Figure 6](#), this study has demonstrated that optimizing the microstructure can effectively increase both S_{ANE} and $z_{ANE}T$ in Nd-Fe-B magnets, paving the way for further advancements in magnet optimization for TEG applications.

CONCLUSIONS

This study addresses a gap in the understanding of how microstructural features can influence the σ_{xx} , κ , and S_{ANE} in the Nd-Fe-B permanent magnets fabricated from rapidly solidified ribbon powders, offering insights into improving S_{ANE} . The findings reveal that S_{ANE} increases by 68%, from $-2.6 \times 10^{-7} \text{ VK}^{-1}$ in the HP state to $-4.4 \times 10^{-7} \text{ VK}^{-1}$ after HD in which grain growth and crystallographic texture are realized without changing the composition of the magnets. S_{ANE} further increases to $-5.0 \times 10^{-7} \text{ VK}^{-1}$ after grain boundary structure and composition change from thin amorphous phase to thick crystalline phase by grain boundary diffusion of Dy-Nd-Cu alloy. The increase in S_{ANE} is primarily due to the reduction of the opposing S_{II} component following HD and GBDP. Owing to the crystallographic texture formation after HD, almost the same transverse thermopower as S_{ANE} is obtained in HD and RE-Cu (RE = Dy-Nd, Nd, and Pr) GBDP Nd-Fe-B magnets at the M_i state (zero H). However, the enhancement in S_{ANE} following GBDP is somewhat counterbalanced by the increase in κ , resulting in a smaller improvement in $z_{ANE}T$. These findings demonstrate that microstructural optimization can effectively enhance the S_{ANE} in ultra-fine grained Nd-Fe-B magnets, providing a promising avenue for advancing materials in applications of transverse

thermoelectrics.

DECLARATIONS

Acknowledgments

The authors thank Xin Tang for valuable discussions and Nozomi Kurata for technical support.

Author's contributions

Investigation, data curation, writing - original draft and editing: Kautsar, Z. H.

Investigation, data curation, writing - review and editing: Madavali, B.

Formal analysis, writing - review and editing: Hirai, T.

Supervision, formal analysis, writing - review and editing: Uchida, K.

Supervision, formal analysis, investigation, writing - review and editing: Sepehri-Amin, H.

Availability of data and materials

The data supporting our findings can be found in the [Supplementary Materials](#).

Financial support and sponsorship

This work was supported by ERATO “Magnetic Thermal Management Materials” (Grant No. JPMJER2201) from Japan Science and Technology Agency (JST).

Conflicts of interest

All authors declared that there are no conflicts of interest.

Ethical approval and consent to participate

Not applicable.

Consent for publication

Not applicable.

Copyright

© The Author(s) 2025.

REFERENCES

1. Ando, F.; Hirai, T.; Uchida, K. Permanent-magnet-based transverse thermoelectric generator with high fill factor driven by anomalous Nernst effect. *APL. Energy*. **2024**, *2*, 016103. [DOI](#)
2. He, R.; Schierming, G.; Nielsch, K. Thermoelectric devices: a review of devices, architectures, and contact optimization. *Adv. Mater. Technol.* **2018**, *3*, 1700256. [DOI](#)
3. Ying, P.; Reith, H.; Nielsch, K.; He, R. Geometrical optimization and thermal-stability characterization of Te-free thermoelectric modules based on MgAgSb/Mg₃(Bi,Sb)₂. *Small* **2022**, *18*, 2201183. [DOI](#)
4. Bu, Z.; Zhang, X.; Hu, Y.; et al. An over 10% module efficiency obtained using non-Bi₂Te₃ thermoelectric materials for recovering heat of <600 K. *Energy. Environ. Sci.* **2021**, *14*, 6506-13. [DOI](#)
5. Ando, F.; Tamaki, H.; Matsumura, Y.; et al. Dual-boost thermoelectric power generation in a GeTe/Mg₃Sb₂-based module. *Mater. Today. Phys.* **2023**, *36*, 101156. [DOI](#)
6. Uchida, K.; Zhou, W.; Sakuraba, Y. Transverse thermoelectric generation using magnetic materials. *Appl. Phys. Lett.* **2021**, *118*, 140504. [DOI](#)
7. Yamauchi, T.; Hamada, Y.; Kurokawa, Y.; Yuasa, H. Anomalous Nernst effect dependence on composition in Fe_{100-x}Rh_x alloys. *Jpn. J. Appl. Phys.* **2022**, *61*, SC1019. [DOI](#)
8. Hamada, Y.; Kurokawa, Y.; Yamauchi, T.; Hanamoto, H.; Yuasa, H. Anomalous Nernst effect in Fe-Si alloy films. *Appl. Phys. Lett.* **2021**, *119*, 152404. [DOI](#)
9. Sakai, A.; Mizuta, Y. P.; Nugroho, A. A.; et al. Giant anomalous Nernst effect and quantum-critical scaling in a ferromagnetic semimetal. *Nat. Phys.* **2018**, *14*, 1119-24. [DOI](#)
10. Reichlova, H.; Schlitz, R.; Beckert, S.; et al. Large anomalous Nernst effect in thin films of the Weyl semimetal Co₂MnGa. *Appl. Phys.*

- Lett.* **2018**, *113*, 212405. DOI
11. Ikhlas, M.; Tomita, T.; Koretsune, T.; et al. Large anomalous Nernst effect at room temperature in a chiral antiferromagnet. *Nat. Phys.* **2017**, *13*, 1085-90. DOI
 12. Li, X.; Xu, L.; Ding, L.; et al. Anomalous Nernst and Righi-Leduc Effects in Mn_3Sn : Berry curvature and entropy flow. *Phys. Rev. Lett.* **2017**, *119*, 056601. DOI
 13. Li, M.; Pi, H.; Zhao, Y.; et al. Large anomalous Nernst effects at room temperature in Fe_3Pt thin films. *Adv. Mater.* **2023**, *35*, 2301339. DOI
 14. He, B.; Şahin, C.; Boona, S. R.; et al. Large magnon-induced anomalous Nernst conductivity in single-crystal MnBi . *Joule* **2021**, *5*, 3057-67. DOI PubMed PMC
 15. Xu, L.; Li, X.; Ding, L.; et al. Anomalous transverse response of Co_2MnGa and universality of the room-temperature $\alpha_{ij}^A/\sigma_{ij}^A$ ratio across topological magnets. *Phys. Rev. B* **2020**, *101*, 180404. DOI
 16. Park, G.; Reichlova, H.; Schlitz, R.; et al. Thickness dependence of the anomalous Nernst effect and the Mott relation of Weyl semimetal Co_2MnGa thin films. *Phys. Rev. B* **2020**, *101*, 060406. DOI
 17. Sakai, A.; Minami, S.; Koretsune, T.; et al. Iron-based binary ferromagnets for transverse thermoelectric conversion. *Nature* **2020**, *581*, 53-7. DOI
 18. Cox, C. D. W.; Caruana, A. J.; Cropper, M. D.; Morrison, K. Anomalous Nernst effect in Co_2MnSi thin films. *J. Phys. D: Appl. Phys.* **2020**, *53*, 035005. DOI
 19. Khadka, D.; Thapaliya, T. R.; Hurtado, P. S.; et al. Anomalous Hall and Nernst effects in epitaxial films of topological kagome magnet Fe_3Sn_2 . *Phys. Rev. Mater.* **2020**, *4*, 084203. DOI
 20. Wuttke, C.; Cagliaris, F.; Sykora, S.; et al. Berry curvature unravelled by the anomalous Nernst effect in Mn_3Ge . *Phys. Rev. B* **2019**, *100*, 085111. DOI
 21. Guin, S. N.; Manna, K.; Noky, J.; et al. Anomalous Nernst effect beyond the magnetization scaling relation in the ferromagnetic Heusler compound Co_2MnGa . *NPG. Asia. Mater.* **2019**, *11*, 116. DOI
 22. Uchida, K.; Hirai, T.; Ando, F.; Sepehri-Amin, H. Hybrid transverse magneto-thermoelectric cooling in artificially tilted multilayers. *Adv. Energy. Mater.* **2024**, *14*, 2302375. DOI
 23. Hirai, T.; Ando, F.; Sepehri-Amin, H.; Uchida, K. I. Hybridizing anomalous Nernst effect in artificially tilted multilayer based on magnetic topological material. *Nat. Commun.* **2024**, *15*, 9643. DOI PubMed PMC
 24. Coey, J. Permanent magnets: plugging the gap. *Scr. Mater.* **2012**, *67*, 524-9. DOI
 25. Coey, J. Perspective and prospects for rare earth permanent magnets. *Engineering* **2020**, *6*, 119-31. DOI
 26. Gutfleisch, O.; Willard, M. A.; Brück, E.; Chen, C. H.; Sankar, S. G.; Liu, J. P. Magnetic materials and devices for the 21st century: stronger, lighter, and more energy efficient. *Adv. Mater.* **2011**, *23*, 821-42. DOI PubMed
 27. Miura, A.; Sepehri-Amin, H.; Masuda, K.; et al. Observation of anomalous Ettingshausen effect and large transverse thermoelectric conductivity in permanent magnets. *Appl. Phys. Lett.* **2019**, *115*, 222403. DOI
 28. Sakuraba, Y.; Hyodo, K.; Sakuma, A.; Mitani, S. Giant anomalous Nernst effect in the $\text{Co}_2\text{MnAl}_{1-x}\text{Si}_x$ Heusler alloy induced by Fermi level tuning and atomic ordering. *Phys. Rev. B* **2020**, *101*, 134407. DOI
 29. Fujiwara, K.; Kato, Y.; Abe, H.; et al. Berry curvature contributions of kagome-lattice fragments in amorphous Fe-Sn thin films. *Nat. Commun.* **2023**, *14*, 3399. DOI
 30. Gautam, R.; Hirai, T.; Alasli, A.; et al. Creation of flexible spin-caloritronic material with giant transverse thermoelectric conversion by nanostructure engineering. *Nat. Commun.* **2024**, *15*, 2184. DOI PubMed PMC
 31. Wang, Z.; Pei, K.; Zhang, J.; et al. Correlation between the microstructure and magnetic configuration in coarse-grain inhibited hot-deformed Nd-Fe-B magnets. *Acta. Mater.* **2019**, *167*, 103-11. DOI
 32. Ramesh, R.; Thomas, G.; Ma, B. M. Magnetization reversal in nucleation controlled magnets. II. Effect of grain size and size distribution on intrinsic coercivity of Fe-Nd-B magnets. *J. Appl. Phys.* **1988**, *64*, 6416-23. DOI
 33. Nothnagel, P.; Müller, K.; Eckert, D.; Handstein, A. The influence of particle size on the coercivity of sintered NdFeB magnets. *J. Magn. Magn. Mater.* **1991**, *101*, 379-81. DOI
 34. Lv, M.; Kong, T.; Zhang, W.; et al. Progress on modification of microstructures and magnetic properties of Nd-Fe-B magnets by the grain boundary diffusion engineering. *J. Magn. Magn. Mater.* **2021**, *517*, 167278. DOI
 35. Cui, W.; Takahashi, Y.; Hono, K. Microstructure optimization to achieve high coercivity in anisotropic Nd-Fe-B thin films. *Acta. Mater.* **2011**, *59*, 7768-75. DOI
 36. Lee, R.; Brewer, E.; Schaffel, N. Processing of neodymium-iron-boron melt-spun ribbons to fully dense magnets. *IEEE. Trans. Magn.* **1985**, *21*, 1958-63. DOI
 37. Croat, J. Manufacture of Nd Fe B permanent magnets by rapid solidification. *J. Less. Common. Met.* **1989**, *148*, 7-15. DOI
 38. Liu, J.; Sepehri-Amin, H.; Ohkubo, T.; Hioki, K.; Hattori, A.; Hono, K. Microstructure evolution of hot-deformed Nd-Fe-B anisotropic magnets. *J. Appl. Phys.* **2014**, *115*, 17A744. DOI
 39. Sepehri-Amin, H.; Ohkubo, T.; Nagashima, S.; et al. High-coercivity ultrafine-grained anisotropic Nd-Fe-B magnets processed by hot deformation and the Nd-Cu grain boundary diffusion process. *Acta. Mater.* **2013**, *61*, 6622-34. DOI
 40. Sepehri-Amin, H.; Liu, L.; Ohkubo, T.; et al. Microstructure and temperature dependent of coercivity of hot-deformed Nd-Fe-B magnets diffusion processed with Pr-Cu alloy. *Acta. Mater.* **2015**, *99*, 297-306. DOI
 41. Sepehri-Amin, H.; Liu, J.; Ohkubo, T.; Hioki, K.; Hattori, A.; Hono, K. Enhancement of coercivity of hot-deformed Nd-Fe-B

- anisotropic magnet by low-temperature grain boundary diffusion of Nd₆₀Dy₂₀Cu₂₀ eutectic alloy. *Scr. Mater.* **2013**, 69, 647-50. DOI
42. Bahl, C. R. H. Estimating the demagnetization factors for regular permanent magnet pieces. *AIP. Advances.* **2021**, 11, 075028. DOI
 43. Breitenstein, O.; Warta, W.; Schubert, M. C. *Lock-in Thermography*. Springer International Publishing, Cham, 2018. DOI
 44. Uchida, K. I.; Daimon, S.; Iguchi, R.; Saitoh, E. Observation of anisotropic magneto-Peltier effect in nickel. *Nature* **2018**, 558, 95-9. DOI
 45. Miura, A.; Masuda, K.; Hirai, T.; et al. High-temperature dependence of anomalous Ettingshausen effect in SmCo₅-type permanent magnets. *Appl. Phys. Lett.* **2020**, 117, 082408. DOI
 46. Wid, O.; Bauer, J.; Müller, A.; Breitenstein, O.; Parkin, S. S.; Schmidt, G. Investigation of the unidirectional spin heat conveyer effect in a 200 nm thin yttrium iron garnet film. *Sci. Rep.* **2016**, 6, 28233. DOI PubMed PMC
 47. Seki, T.; Iguchi, R.; Takanashi, K.; Uchida, K. Visualization of anomalous Ettingshausen effect in a ferromagnetic film: direct evidence of different symmetry from spin Peltier effect. *Appl. Phys. Lett.* **2018**, 112, 152403. DOI
 48. Das, R.; Iguchi, R.; Uchida, K. Systematic investigation of anisotropic Magneto-Peltier effect and anomalous Ettingshausen effect in Ni thin films. *Phys. Rev. Appl.* **2019**, 11, .034022. DOI
 49. Campos MF, Romero SA, de Castro JA. Estimation of texture and anisotropy field in a NdDyFeCoB magnet by magnetic measurements at the perpendicular direction. *J. Magn. Magn. Mater.* **2022**, 564, 170119.
 50. Lee, Y.; Huang, G.; Shih, C.; Chang, W.; Chang, H.; You, J. Coercivity enhancement in hot deformed Nd₂Fe₁₄B-type magnets by doping low-melting RCu alloys (R = Nd, Dy, Nd + Dy). *J. Magn. Magn. Mater.* **2017**, 439, 1-5. DOI
 51. Cui, B. Z.; Zheng, L. Y.; Marinescu, M.; Liu, J. F.; Hadjipanayis, G. C. Textured Nd₂Fe₁₄B flakes with enhanced coercivity. *J. Appl. Phys.* **2012**, 111, 07A735. DOI
 52. Hirotsawa, S.; Matsuura, Y.; Yamamoto, H.; Fujimura, S.; Sagawa, M.; Yamauchi, H. Magnetization and magnetic anisotropy of R₂Fe₁₄B measured on single crystals. *J. Appl. Phys.* **1986**, 59, 873-9. DOI
 53. Hu, C.; Xia, K.; Fu, C.; Zhao, X.; Zhu, T. Carrier grain boundary scattering in thermoelectric materials. *Energy. Environ. Sci.* **2022**, 15, 1406-22. DOI
 54. Dong, H.; Wen, B.; Melnik, R. Relative importance of grain boundaries and size effects in thermal conductivity of nanocrystalline materials. *Sci. Rep.* **2014**, 4, 7037. DOI PubMed PMC
 55. Cahill, D. G.; Watson, S. K.; Pohl, R. O. Lower limit to the thermal conductivity of disordered crystals. *Phys. Rev. B.* **1992**, 46, 6131. DOI
 56. Cahill, D. G.; Pohl, R. O. Lattice vibrations and heat transport in crystals and glasses. *Annu. Rev. Phys. Chem.* **1988**, 39, 93-121. DOI
 57. Sakuma, A.; Suzuki, T.; Furuuchi, T.; Shima, T.; Hono, K. Magnetism of Nd-Fe films as a model of grain boundary phase in Nd-Fe-B permanent magnets. *Appl. Phys. Express.* **2016**, 9, 013002. DOI
 58. Stankiewicz, J.; Bartolomé, J. Magnetotransport properties of Nd₂Fe₁₄B. *Phys. Rev. B.* **1999**, 59, 1152. DOI
 59. Ding, L.; Koo, J.; Xu, L.; et al. Intrinsic anomalous Nernst effect amplified by disorder in a half-metallic semimetal. *Phys. Rev. X.* **2019**, 9, 041061. DOI
 60. Behnia, K.; Aubin, H. Nernst effect in metals and superconductors: a review of concepts and experiments. *Rep. Prog. Phys.* **2016**, 79, 046502. DOI PubMed
 61. Zhou, W.; Masuda, K.; Sakuraba, Y. Origin of negative anomalous Nernst thermopower in Mn-Ga ordered alloys. *Appl. Phys. Lett.* **2021**, 118, 152406. DOI